

RESEARCH ARTICLE

Sensory Processing

## Model-based characterization of the selectivity of neurons in primary visual cortex

 Felix Bartsch,<sup>1</sup> Bruce G. Cumming,<sup>2</sup> and  Daniel A. Butts<sup>1</sup>

<sup>1</sup>Program in Neuroscience and Cognitive Science, University of Maryland, College Park, Maryland and <sup>2</sup>Laboratory of Sensorimotor Research, National Eye Institute, NIH, Bethesda, Maryland

### Abstract

Statistical models are increasingly being used to understand the complexity of stimulus selectivity in primary visual cortex (V1) in the context of complex time-varying stimuli, replacing averaging responses to simple parametric stimuli. Although such models often can more accurately reflect the computations performed by V1 neurons in more natural visual environments, they do not by themselves provide insight into V1 neural selectivity to basic stimulus features such as receptive field size, spatial frequency tuning, and phase invariance. Here, we present a battery of analyses that can be directly applied to encoding models to link complex encoding models to more interpretable aspects of stimulus selectivity. We apply this battery to nonlinear models of V1 neurons recorded in awake macaque during random bar stimuli. In linking model properties to more classical measurements, we demonstrate several novel aspects of V1 selectivity not available to simpler experimental measurements. For example, this approach reveals that individual spatiotemporal elements of the V1 models often have a smaller spatial scale than the neuron as a whole, resulting in nontrivial tuning to spatial frequencies. In addition, we propose measures of nonlinear integration that suggest that classical classifications of V1 neurons into simple versus complex cells will be spatial-frequency dependent. In total, rather than obfuscate classical characterizations of V1 neurons, model-based characterizations offer a means to more fully understand their selectivity, and link their classical tuning properties to their roles in more complex, natural, visual processing.

**NEW & NOTEWORTHY** Visual neurons are increasingly being studied with more complex, natural visual stimuli, and increasingly complex models are necessary to characterize their response properties. Here, we describe a battery of analyses that relate these more complex models to classical characterizations. Using such model-based characterizations of V1 neurons furthermore yields several new insights into V1 processing not possible to capture in more classical means to measure their visual selectivity.

modeling; V1; vision

### INTRODUCTION

The activity of neurons in primary visual cortex (V1) sets the foundation for the cortical processing of vision. Thus, detailed characterization of their stimulus selectivity is of great intrinsic utility. Since the initial discovery of their basic selectivity to oriented bars (1), most V1 neurophysiology has used precise manipulations of simple parametric stimuli such as flashed or drifting gratings (2–4) to make measurements of dominant aspects of V1 visual selectivity, such as receptive field (RF) size and location, orientation tuning, and spatial frequency and temporal frequency tuning (1, 5–7). Because how V1 processes these simple parametric stimuli

has limited power in predicting their responses to more complex time-varying stimuli (8–10), a large number of increasingly sophisticated models have been used to understand their responses to more complex stimuli (8), using techniques ranging from spike-triggered covariance (11, 12) up through modern machine-learning methods (e.g., see Ref. 13). Although the necessity of more sophisticated models to capture neural computation in complex stimulus contexts suggests that these previous measures of V1 selectivity offer an incomplete picture of its processing of natural vision, it is not clear whether more sophisticated approaches are simply measuring different aspects of processing, and exactly what is gained by them relative to more canonical measurements.

Indeed, the success of more sophisticated models in explaining V1 neural responses is often at the expense of the interpretability that defined more canonical approaches to characterizing V1 neurons (8). Likewise, few studies analyzing models to gain insight into neural properties have attempted to directly relate modern nonlinear modeling approaches to classical measures of cell (although see Ref. 14). Here, we focus on the most interpretable of these modern models: “subunit” models such as the LNLN cascade (15–17), which consist of a linear combination of nonlinear spatiotemporal stimulus filters (or “subunits”) that are each selective to a particular stimulus feature that contributes to the neuron’s response (15, 17–19). The array of spatiotemporal filters generated by these models are determined by optimization of model parameters using data recorded during any sufficiently general spatiotemporally varying visual stimulus paradigm and captures the set of stimulus features that affect the neuron’s response. We present several measures that can then be derived from the resulting models, which can be directly related to canonical aspects of neural tuning while capturing other interpretable aspects of its selectivity. Notably, while we apply these measures to the models measured in this particular context, such measures can be generalized to any “image-computable” model of V1 neurons (8). Because such more sophisticated characterizations of V1 processing implicitly capture V1 neural selectivity to multiple features as well as interactions between selectivity to related features, the resulting descriptions of V1 computation go beyond what can be achieved with simple parametric stimuli, and set a new bar for measurements of V1 neural selectivity.

## MATERIALS AND METHODS

### Neurophysiology Experiments

We used previously collected recordings, as described in detail in Ref. 20. Briefly, multi-electrode recordings were made from primary visual cortex (V1) of two awake head-restrained male rhesus macaques (*Macaca mulatta*; 13- to 14-yr old) while the animals performed a simple fixation task, where they were required to maintain gaze within a small window around a fixation target to obtain a liquid reward after each completed 4-s trial. Eye position was monitored continuously using scleral search coils in each eye, sampled at 600 Hz, and a model-based eye-position correction algorithm (see *Model-Based Eye Tracking*) was applied to accurately recover eye position at sufficiently high spatial resolution (20, 21). Trials during which the monkey broke fixation were discarded from analysis. In addition, the first 200 ms and last 50 ms of each trial were excluded from analysis to minimize the impact of onset transients.

### Recordings

In one animal, we implanted a 96-electrode planar Utah array (Blackrock Microsystems; 400  $\mu\text{m}$  spacing), in the other, a linear electrode array (V-probe, Plexon; 24 contacts, 50  $\mu\text{m}$  spacing) was passed through the dura at the start of each day. Spike waveforms were detected online using Spike2 software (Cambridge Electronic Design) and recorded at 32 kHz (Utah array) or at 40 kHz (V-Probe) sampling rate.

Single units (SUs) were identified through offline spike-sorting with custom software. Spike clusters were modeled using Gaussian mixture distributions that were based on several different spike features, including principal components, voltage samples, and template scores. The features providing the best cluster separation were used to cluster single units. Cluster quality was quantified using a variety of measures including “L-ratio,” “isolation distance,” as well as a variant of “d-prime.” Only spike clusters that were well isolated using these measures—confirmed by visual inspection—and had average firing rates during stimulus presentation of at least five spikes per second were used for analysis. Voltage signals were also separately low-passed at 100 Hz and used to compute the inverse current-source density (iCSD) profile of each recording, to categorize each isolated single unit by layer (22, 23). All protocols were approved by the Institutional Animal Care and Use Committee and complied with Public Health Service policy on the humane care and use of laboratory animals.

### Stimuli

We presented a ternary bar noise stimulus, consisting of random patterns of black, white, and gray bars (matching the mean luminance of the screen). These stimuli were displayed on a cathode ray tube (CRT) monitor at a 100 Hz refresh rate; the monitors subtended  $24.3^\circ \times 19.3^\circ$  of visual angle. RFs were manually mapped online, and stimuli were then centered over the mapped RF location. Stimuli consisted of 36 individual bars that had a width of  $0.057^\circ$  for the Utah array recordings and ranged from  $0.038^\circ$  to  $0.1^\circ$  for the linear array recordings, depending on the RF sizes of the recorded neurons. The bar length was adjusted to yield square stimulus patches such that stimuli subtended between  $1.368^\circ$  and  $3.6^\circ$ . Bar patterns were uncorrelated in space and time. The probability of a given bar being non-gray (i.e., black or white) was set to 12% (i.e., 88% gray, relatively sparse), although in several experiments we used a denser distribution (33% gray), which yielded similar results. For the linear array recordings, the orientation of the bars was chosen to be within  $15^\circ$  of the preferred orientation of the majority of units recorded in a given session. In Utah array recordings, where the neurons typically had a full range of preferred orientations due to being located across multiple orientation columns, we performed the experiments with two different bar orientations (vertical and horizontal) that alternated on a block-by-block basis, where blocks were  $\sim 10$  min of recording time in duration. In this case, we modeled the orientation that best drove neural activity, and the properties of cells recorded using this approach were comparable with those recorded during presentation of more optimally oriented bar stimuli.

### Model-Based Eye Tracking

Due to fixational eye movements, the stimulus projected on the retina is shifted over time, which can result in misestimation of model parameters (20, 21). As a result, we estimated the precise position of the eye perpendicular to our one-dimensional stimuli as a function of time using model-based eye tracking (20). This algorithm uses the observed

firing rates during each fixation period to estimate the probability of each potential eye position, and—with enough neurons simultaneously recorded—these probabilities can be combined to accurately infer the most likely eye position, which can be accurate to arc-min resolution. Using this estimated position, we then adjusted the presented stimulus by the eye shifts and used the resulting adjusted stimulus to fit the models, as described in detail in Ref. 20.

## Model Structure

We used the Nonlinear Input Model (NIM) to model V1 neurons (15). The NIM (Fig. 1A) operates on the stimulus  $\mathbf{s}(t)$  with a number of linear-nonlinear (LN) subunits, each consisting of a stimulus filter  $\mathbf{k}$  (Fig. 1B) and a rectifying nonlinearity  $f(\cdot)$ . Subunit outputs are then weighted by either  $+1$  or  $-1$  (depending on whether each is excitatory or inhibitory, respectively), and summed together and passed through a

final spiking nonlinearity  $F[\cdot]$  to result in a predicted firing rate  $r(t)$ : given stimulus  $\mathbf{s}(t)$  is given as:

$$r(t) = F\left[\sum_n w_n f_n(\mathbf{k}_n \cdot \mathbf{s}(t))\right] \quad (1)$$

where  $w_n$  is  $+1$  or  $-1$  as described earlier. We use a “Relu” (rectified linear) function for the subunit nonlinearity  $f(\cdot)$ , and a softplus nonlinear function for the spiking nonlinearity:  $F(x) = \log[1 + \exp(x)]$  as in our previous work (15).

We initially fit NIMs to each neuron using standard maximum a posteriori optimization in the context of sparseness (L1) and smoothness (Laplacian) regularization. Both the number of subunits and the regularization parameters were optimized through nested cross-validation, as described previously (8, 15). We then leveraged the resulting collection of models to yield additional model improvements, using dimensionality reduction on the spatiotemporal filters

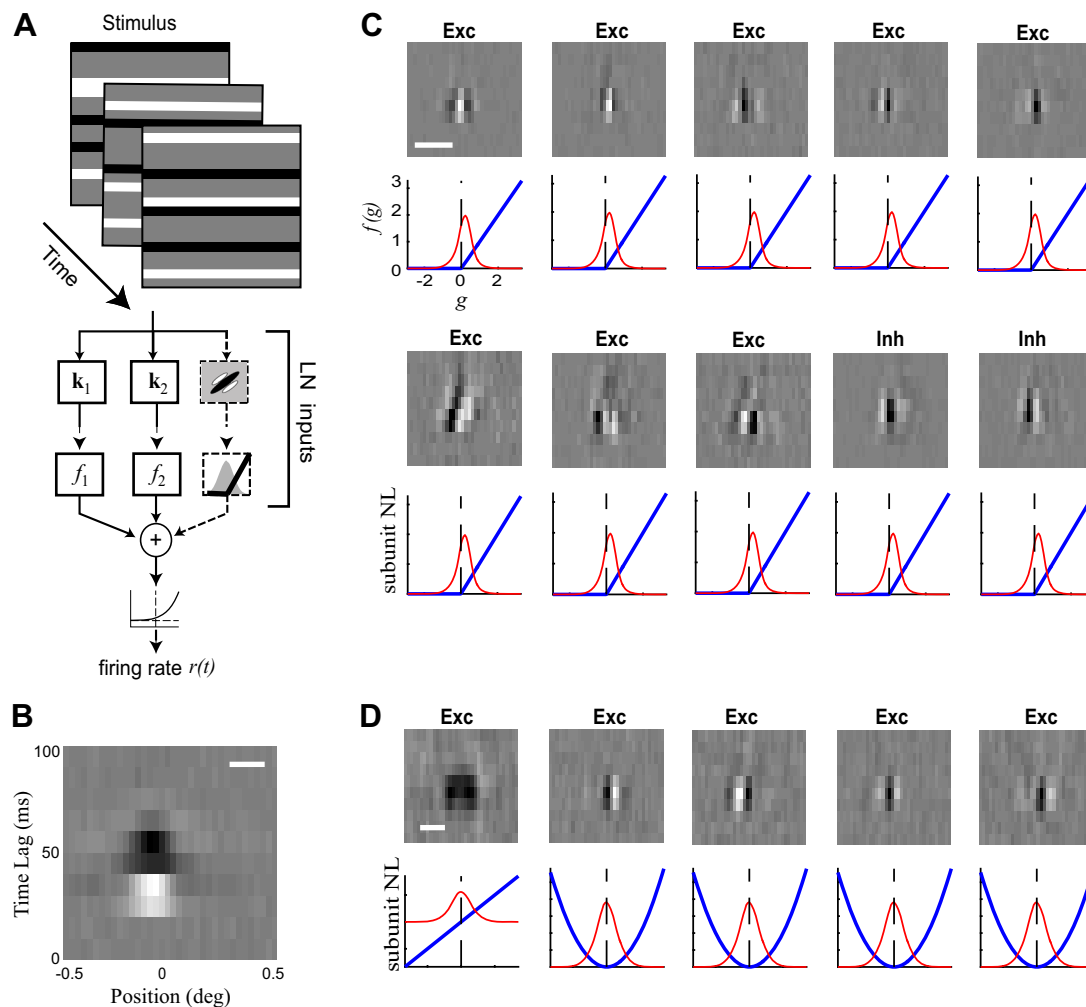


**Figure 1.** Extracting receptive field (RF) components using stimulus models. **A:** schematic of the linear-nonlinear-linear-nonlinear (LNLN) cascade stimulus processing models. Stimulus frames (top) are passed through spatiotemporal filters  $\mathbf{k}_i$ , the outputs of which are then passed through a rectifying nonlinearity (NL). The outputs of these “LN subunits” are then summed to give the “generating signal”  $g(t)$ , which is transformed into a firing rate by the spiking nonlinearity (bottom). In the case of the principal component nonlinear input model (PCNIM), filters  $\mathbf{k}_i$  were not fit using the full stimulus space, but rather its low-dimensional projection into the space outlined by the principal components. After fitting, they were retranslated into full space for interpretation. **B:** example spatiotemporal filter. **C:** example of filters fit using the PCNIM with eight excitatory (Exc) and two suppressive (Inh) filters. The nonlinearity associated with each filter is shown below (blue), as is the distribution of stimulus projections onto each filter (red). **D:** example of filters fit by a GQM architecture with four excitatory quadratic filters. Nonlinearities are again displayed below each filter in blue. The scale bars in B–D indicate 0.1° of visual angle.

pooled across all models. Specifically, this database (over all neurons in the data set fit using standard NIMs) consisted of 2,061 filters, which were then centered to remove any spatial shifts between them. We computed the principal components (PCs) of this filterbank, finding that 80% of its variance could be explained by the first 50 PCs, with diminishing returns from including more (see Fig. A1A). We then applied these top 50 filters to the spatiotemporal stimulus  $\mathbf{s}$ , resulting in a 50-dimensional “dimensionality-reduced” stimulus in place of the 360-dimensional “full” stimulus that was composed of 36 spatial dimensions and 10 lags.

The resulting dimensionality-reduced stimulus was used in Eq. 1 in place of the full stimulus, and NIMs were refit using the filtered, dimensionality-reduced stimulus, resulting in principal component NIMs, or PCNIMs. The fit model subunits thus had a set of coefficients corresponding to the weights on the PCs, and the full spatiotemporal filters could be recovered by matrix multiplication. This allowed for the potential inclusion of many more subunits without overfitting (see *Model Parameter Optimization*). Furthermore, because the PCs did not reflect noise in the filter estimation that was not shared among many filters, it was not necessary to apply any regularization in subsequent stages of fitting. Representing model filters using PCA yielded better model performance (Fig. A1C) than the standard NIM approach, including finding more subunits that improve model performance that would have been suppressed by regularization penalties for the standard NIM.

In addition to using the standard structure of the NIM with rectified subunits, we also compared LNLN cascades with linear and quadratic subunit nonlinearities  $f_n(\cdot)$  (Eq. 1) (15, 16, 18) (Fig. 1C). This “quadratic” model is also commonly used to model V1 neurons because it embodies the “energy model” (24, 25), although it is less flexible in approximating more general nonlinearities (8, 15). We applied a subspace approach to fitting quadratic models as well but found that both full and subspace quadratic models converged on equivalent subunit structures with similar cross-validated performance. As a result, we report results from the more straightforward quadratic model fits that do not rely on the filter subspace.

### Model Parameter Optimization

The parameters of the filters are fit and optimized through a maximum-likelihood approach as described in detail (15). This approach maximizes the log-likelihood (LL) of the model, which is given by the equation

$$LL = \sum_i (R_{\text{obs}}(t) \log r(t) - r(t)) \quad (2)$$

where  $r(t)$  is the predicted firing rate and  $R_{\text{obs}}(t)$  is the observed spike count, assuming a Poisson noise model. The goodness of fit of the models is assessed using fivefold cross validation: with model parameters fit using 80% of the data, and performance assessed using the LL of the models on the remaining 20% of the data.

### Model Hyperparameter Optimization

In addition to the parameters corresponding to the spatiotemporal filters, each model had several “hyperparameters” corresponding to other aspects of the model architecture,

including the number of filters used and the ratio of excitatory to inhibitory filters ( $E-I$  ratio). The number of filters and  $E-I$  ratio were determined through nested cross-validation across a range of possible combinations, refitting model parameters for each new combination and choosing the combination yielding the best cross-validated performance. Note that because subunits were fit in a subspace, they inherited the regularization of the models that were used to generate the filter subspace. When fitting quadratic models, regularization hyperparameters were optimized through nested cross-validation using the same process used to generate the models used for the NIM models that filter subspace was based on.

### Estimating Spatial Frequency Tuning Using Forward Correlation

To compare model-based measures of spatial frequency (SF) tuning to a model-free measure, we used forward correlation. We first extracted spatial frequency spectra of each stimulus frame via fast-Fourier transform (FFT) and ranked frames by power in each resulting frequency bin. For each frequency, we then extract two peristimulus time histograms (PSTHs) corresponding to frames with power at that frequency in the top 30th percentile and in the bottom 30th percentile. The difference between these two PSTHs provides a model-free estimate of the neuron’s SF tuning directly comparable with those obtained using classical measures of SF tuning. We defined the cell’s preferred frequency as the peak of this curve.

### Estimating Nonlinearity across Space Using Forward Correlation

We also used forward correlation to validate measures of nonlinearity, computing the average response following the presentation of black, white, or gray bars at a given spatial position:  $\bar{r}_{\text{black}}(x)$ ,  $\bar{r}_{\text{white}}(x)$ , and  $\bar{r}_{\text{gray}}(x)$ , respectively. As described in the text, the phase-reversal correlation as a function of spatial position is then given by:

$$\text{PRFC}(x) = \frac{|\bar{r}_{\text{black}}(x) - \bar{r}_{\text{white}}(x)|}{2 \max[\bar{r}_{\text{black}}(x) - \bar{r}_{\text{gray}}(x), \bar{r}_{\text{white}}(x) - \bar{r}_{\text{gray}}(x)]}.$$

This measure can also be summed across space, weighted by the spatial power (cumulative variance of model filters across time, as described in the results), to result in a single phase-reversal forward correlation difference (PRFC) measure for a given neuron.

## RESULTS

### Estimation of a Neuron’s Spatiotemporal Feature Space

To characterize the stimulus processing of V1 neurons, we fit the nonlinear input model (NIM) (15) to a database of 122 V1 neuron responses recorded in the context of noise stimuli consisting of ternary bars aligned to preferred orientation (Fig. 1A) (15, 20) (see MATERIALS AND METHODS). The resulting subunit model of a given V1 neuron provides a set of spatiotemporal stimulus filters that modulate the neuron’s response, as well as a positive or negative weight corresponding to whether the feature was excitatory or suppressive (Fig. 1B). As described earlier, these model components (Fig. 1C)



contain rich information about the selectivity of the neuron being modeled, and here we are interested in analyzing the properties of these filters to extract such information.

We first analyzed the spatial profile of the filters: computing the amount of power (i.e., variance across time lag) at each spatial position, which defines the spatial profile for each spatiotemporal filter (Fig. 2, A and B). The overall spatial profile of the neuron is then defined as the average of its filter profiles, weighted by the relative contribution of each filter's output to the overall predicted firing rate (Fig. 2B, bottom). To associate a single "width" to a given spatial profile, we defined the width of a given profile using the spatial extent between 30% and 70% of the cumulative spatial power is under the profile curve. The same procedure was

applied to assess each neuron's temporal profile by computing power across spatial positions at each time lag; we define temporal onset and offset of each temporal profile using the same cumulative power thresholds as were used for the spatial profiles.

This analysis reveals that, in a large fraction of neurons, there was a significant difference between the extent of each neuron's summed spatial profile and those of its individual subunits. Across the population, 31/122 cell RFs were composed of filters with a mean width less than 75% of the total RF width (Fig. 2C). This discrepancy can be explained by a scatter of the locations of a given neuron's filters (Fig. 2B), such that the full profile of the neuron results from the combination of the spatial extent of its component subunits and

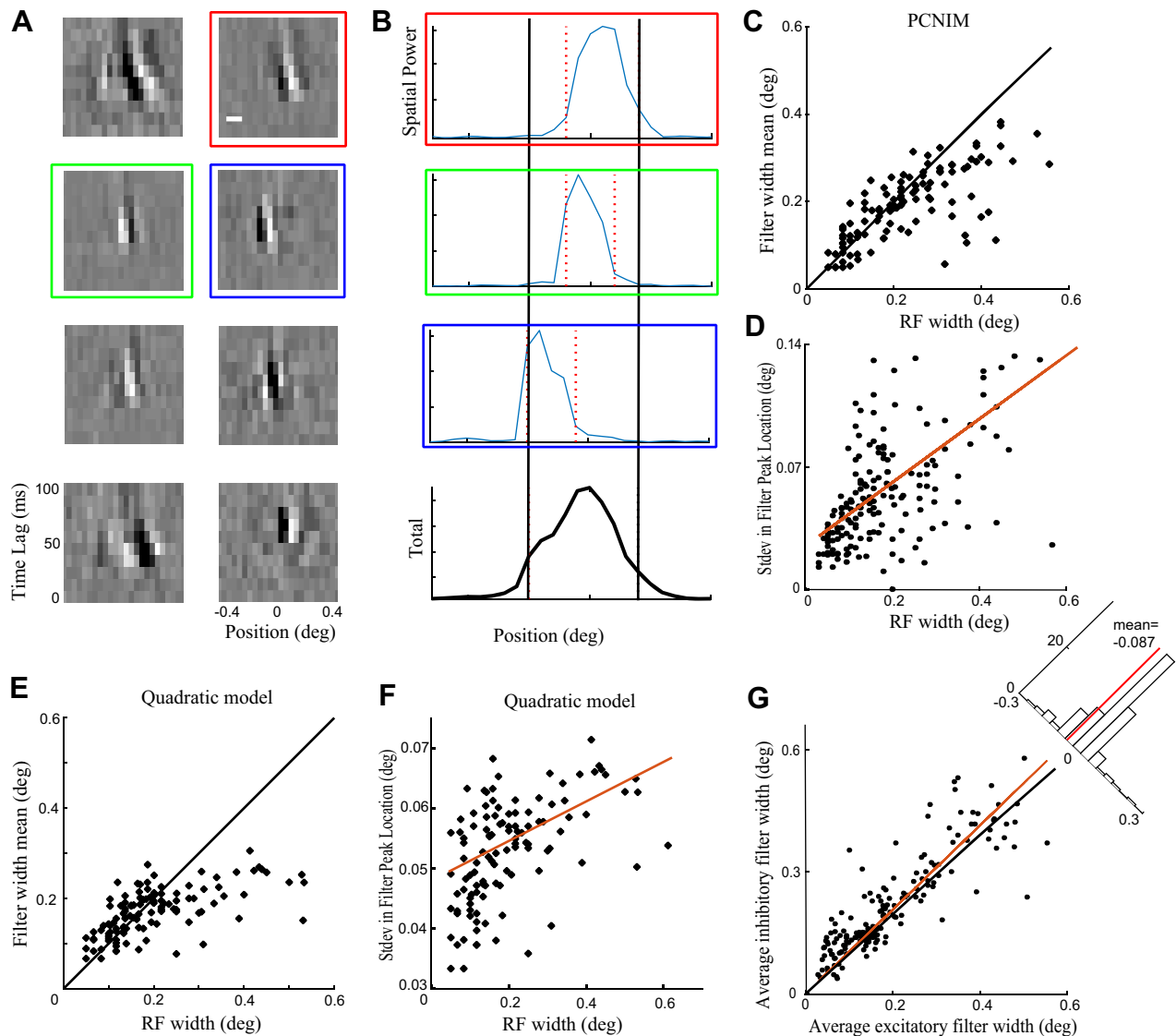


**Figure 2.** The principal component nonlinear input model (PCNIM) reveals high-resolution receptive field (RF) components. **A:** the eight most highly weighted subunit filters for an example neuron, plotted as a function of spatial position (horizontal axis) and temporal lag (vertical axis). **B:** three example spatial power profiles (top) for the highlighted filters (colored boxes) in **A**, compared with the total spatial power profile of the model (black, bottom). Vertical lines indicate the edges of each filter, which is used to determine filter width. **C:** population results comparing the RF width (i.e., width of the total spatial power profile of each neuron) with its mean subunit filter width. **D:** population results comparing RF width and standard deviation of filter locations in excitatory filters, demonstrating that neurons with larger RFs typically have more spatial scatter in the locations of individual filters. **E** and **F:** same as **C** and **D**, respectively, showing mean and standard deviation of filter widths in quadratic model fits. **G:** average width of each model's excitatory and inhibitory filters. Inhibitory filters are overall wider than excitatory filters.

the spatial scatter of these elements. This model-based observation is not readily accessible using direct experimental measurements of RF spatial potential and scale, which produce a single scale and location or preferred phase (25–28).

This observed scatter is unlikely to be caused by our eye-tracking procedure. First, the amount of scatter is neuron-dependent: neurons with small RFs display less scatter, even though inaccurate eye tracking should make scattering of the filters in such highly localized RFs more salient and disproportionately broaden them. Second, we have already corrected for eye-position estimates in the data we use using our model-based eye-tracking procedure as previously reported (20), and the observed scatter is at a much larger scale than the arcminute accuracy of this procedure. Finally, the spatial scatter of subunits is observed in our quadratic model fits (Fig. 2F), as well as in previous studies using other data sets and modeling approaches (e.g., spike-triggered covariance) (11, 29), suggesting that it is not dependent particular choice of model architecture.

Because individual subunits in the NIM are rectified, subunits are implicitly either excitatory (only generating positive or zero output) or suppressive (with a negative weight so its output can only be less than or equal to zero) (15). Such computational distinctions are difficult to assess using classical characterization methods and reveal systematic differences in the selectivity of putative excitatory and inhibitory elements. For example, suppressive subunits typically had an increased width compared with excitatory subunits (Fig. 2G; sign-rank test,  $P = 0.0021$ ). This finding is consistent with intracellular recordings that found that the tuning of inhibitory V1 neurons typically has broader spatial profiles than excitatory V1 neurons (30).

To verify that our observations were not dependent on the specific form of the model, we applied the same analysis to model fit using quadratic subunits (see Fig. 1D for an example model) (15, 16, 20). Measurements we applied to the quadratic models, in general, displayed the same overall trends for filter width (Fig. 2E) and scatter in subunit location (Fig. 2F) as the PCNIM, indicating that these results do not depend solely on our model architecture. The fact that filter scatter appears more pronounced in the NIM can be explained by the quadratic model's arrangement of filters into quadrature pairs that approximates spatial invariance of V1 neuron selectivity (10, 14, 29). Because the quadratic models also underperformed the NIM at predicting neural responses (Fig. A1D), we take this as an indication that one aspect of the increased flexibility with the NIM as a general function approximator (8, 31) is its ability to identify more spatially localized feature selectivity, and that this more localized feature selectivity allows us to more clearly see trends present in the quadratic models.

### Measuring Spatiotemporal Selectivity

The dominant conception of V1 neuron selectivity is that it extracts local information about the spatiotemporal content of the stimulus (24, 25), which is why most classical tests of V1 tuning involve measuring its responses to gratings. Here, we can instead extract information about such tuning by Fourier analysis of the model subunits.

Applying two-dimensional Fourier transforms to each subunit (32) yields a two-dimensional power frequency spectrum (Fig. 3A). Summing this spectrum along either axis generates a tuning curve representing the subunit's selectivity to either spatial or temporal frequency. We define the neuron's preferred frequency by the peaks of the relevant subunit spectra. To then determine the model's overall frequency tuning, we average the tuning spectra across subunits (again weighted by each subunit's contribution to the model output) (Fig. 3B). The resulting tuning curves, as well as peak tuning measures, can be directly compared with classical measures, while also allowing them to be decomposed into each subunit's contribution.

To validate the model-based measures with experimental data in the absence of direct measurements of the classical tuning curves using gratings, we used a model-free estimation of spatial frequency tuning using forward-correlation of the spike train of each cell (33, 34), where we extracted the spatial frequency components of each stimulus frame and identified the frequency components most correlated with the observed neural response (see MATERIALS AND METHODS). In applying this procedure to both the observed and the model-predicted firing rates, we found that the two agree well (Fig. 3D) as statistical tests did not detect any difference in distributions (paired  $t$  test,  $P = 0.8577$ ), indicating that the models are successfully capturing the cell's SF tuning.

Model-based characterization also can address how SF tuning relates to other properties in our models. For example, inhibitory subunits generally have selectivity to lower SFs (Fig. 3C, sign-rank test,  $P = 0.0061$ ), in line with previous results indicating that inhibitory inputs into V1 tend to act on broader spatial scales (30, 35, 36). In addition, we found a positive relationship between subunit SF selectivity and latency (Fig. 3E, Pearson's correlation,  $r = 0.3407$ , 95% CI = [0.1656, 0.4950],  $P = 0.0002$ ), consistent with the study by Mazer et al. (37), indicating that low-frequency features have lower onset latencies and thus may be processed faster.

Using a similar approach applied to the full spatiotemporal spectra, we inferred V1 neuron direction selectivity (DS) from our models by extracting the direction selectivity index (DSI) (38) from each filter's two-dimensional fast Fourier transform (2DFFT) (see Fig. 3A, red lines in *bottom*). We found that subunits of the same model exhibit a variety of spatial frequency sensitivities and DS strengths (Fig. 3G), suggesting that some direction-selective cells will be modulated by stationary inputs. We additionally tested for relationships between DS strength and other tuning properties including SF selectivity and RF size but did not find significant relationships.

### Model-Based Characterization of SF Tuning

Having established model-based measures of spatiotemporal selectivity, we can now compare to more classical ways of estimating SF tuning using drifting grating stimuli (39, 40) to learn how selectivity to SF might be generated. One advantage of model-based approaches is that the models are “image-computable,” meaning that we can simulate the responses of the model to arbitrary stimuli. Although our data set did not include recordings of responses to drifting gratings, we used the models of our sample cells to

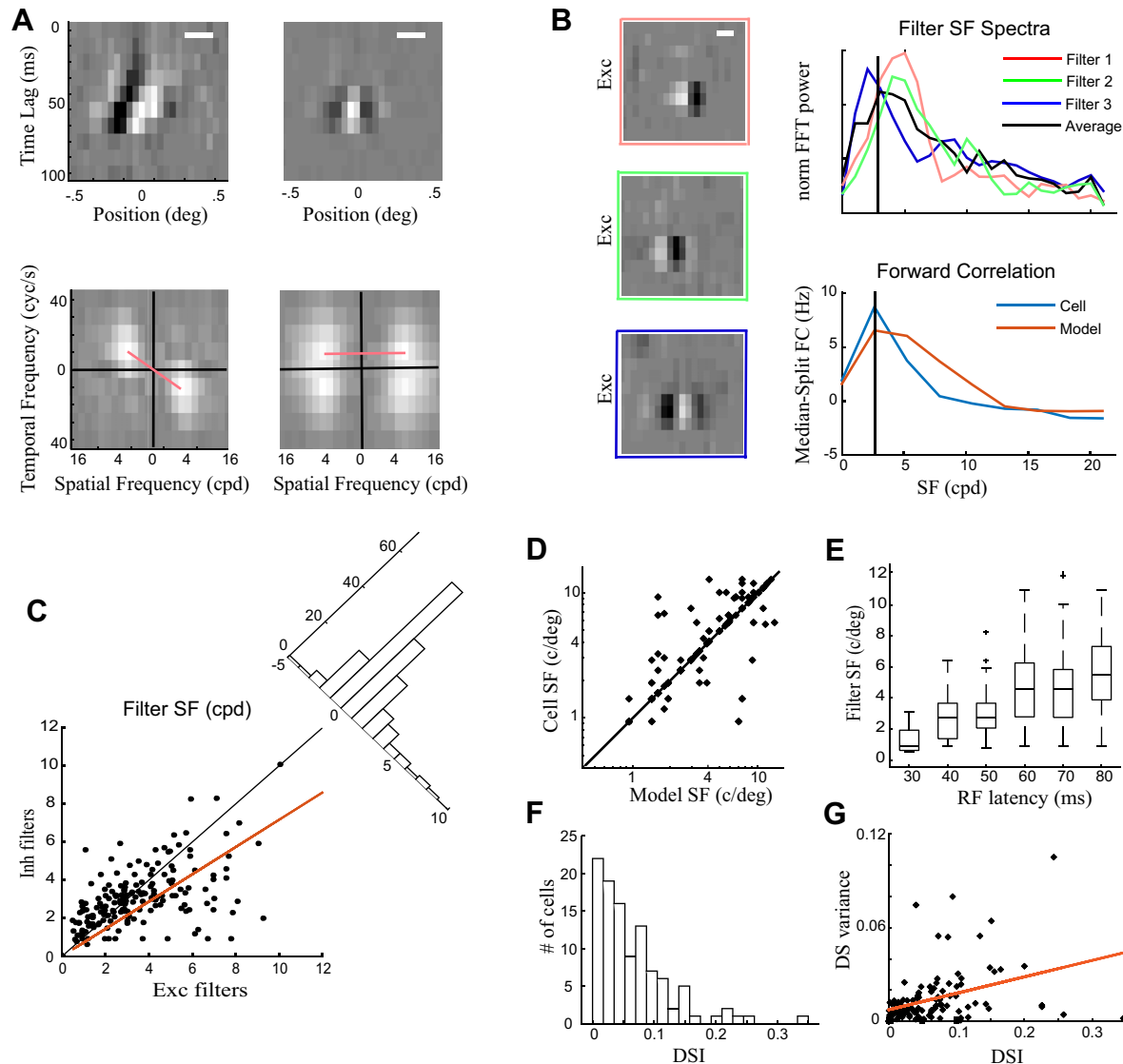


**Figure 3.** Extracting spatial, temporal, and spatiotemporal feature selectivity from models. *A*, top: example filters demonstrating direction selectivity (left) and a nondirection selective filter (right). Scale bars indicate 2° of visual angle. Bottom: two-dimensional FFT (2DFFT) spectra of the above filters. Peaks in the spatial and temporal dimensions are extracted as a measure of frequency tuning preference of the filter. A slope can be fit to the peak locations of the 2DFFT spectrum (red line); this slope is perpendicular to the direction a filter is selective to and can thus be used to estimate direction and velocity tuning, while a 0 slope indicates a filter tuned to static feature (right). In addition, the difference in total power in the top left and top right quadrants of the 2DFFT spectrum can be used to quantify the direction selectivity index (DSI); this measure yields both the direction the cell is selective to, and the strength of its direction selectivity. *B*, left column: example filters. Right column, top: spatial frequency (SF) spectra extracted from the 2DFFT of each filter shown to the left. Each filter tuning curve corresponds to the filter in the left column outlined with the same color. The weighted mean across all filters (weighted by the filter contribution to the model output) is shown in black. Right column, bottom: frequency spectrum of the same cell estimated using forward correlation. Black vertical lines indicate the peak frequency. *C*: differences in spatial frequency tuning of excitatory and inhibitory filters from each model across our population. Excitatory filters are on average tuned to higher spatial frequencies. *D*: preferred spatial frequency as estimated by the model-free forward correlation using observed firing rate and the model prediction. The two measures highly agree, further validating our model approach. *E*: filter spatial frequency preference binned by the filter's onset latency. There is a positive correlation between filter onset delay and spatial frequency tuning. *F*: histogram of DSI values across our sample. *G*: variability in DSI of each filter of a given model versus the model's overall DSI. DS, direction selectivity; Exc, excitatory; FC, forward correlation; FFT, fast-Fourier transform; RF, receptive field.

simulate their firing rates in response to static and drifting gratings and measured the F0 (mean) and F1 (modulation depth) components of the response to each grating frequency (Fig. 4B, solid lines show the responses of the model displayed in Fig. 4A, left) and compared those to our purely model-based estimates of SF preference. This led to a surprise: for some models (27/122), the predicted preferred SF tuning in the context of gratings of the full simulated model was a much lower frequency than that

predicted by the model-based measures that were derived from the filters themselves, as described earlier. Closer inspection of these cells' SF tuning curves revealed two peaks both in their F0 and F1 spectra, with the low-frequency peak in the F1 spectrum indicating the highest response. Normally, the low-SF F1 peak being the largest response would be interpreted as indicating a simple cell tuned to a low SF. However, the F1 outputs of individual filters showed that all were preferentially tuned to higher

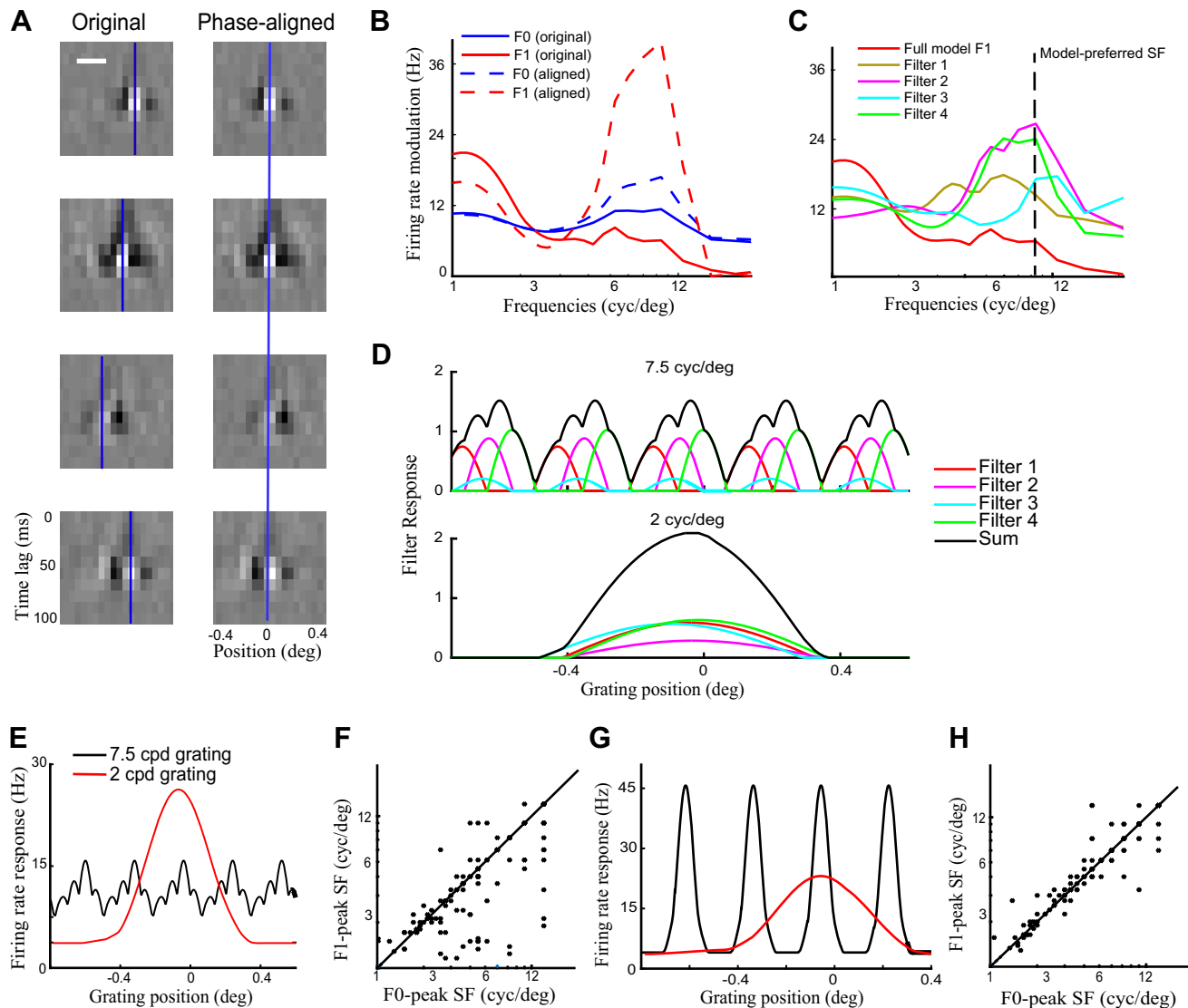


**Figure 4.** Responses to gratings by individual filters and the whole model. **A:** example model of a cell displaying envelope tuning. The four spatiotemporal filters with the highest model contribution are displayed on the *left*, while the same filters following phase alignment are displayed on the *right*. Blue vertical lines indicate the positive phase peak of the Gabor function used to fit the filter. **B:** F0 (blue) and F1 (red) responses to simulated gratings for the original and aligned model's simulated responses to grating stimuli. **C:** F1-based spatial frequency (SF) tuning curves of individual filters and the whole cell estimated using simulated responses of the model to standard grating stimuli. The vertical line indicates the model-estimated SF tuning. **D:** responses over time to a high-frequency (HF) 6 cpd grating (*top*) and a low-frequency (LF) 1.5 cpd grating (*bottom*) by individual filters (colored lines) and their sum (black line). The HF grating drives individual filters well, but the cell's overall phase invariance means that the individual responses do not sum, whereas the LF grating at the envelope frequency drives all filters simultaneously. **E:** original model output in response to LF and HF gratings over time. The sum of weaker modulation by the LF grating generates a larger response than the individual responses of each filter to the HF grating. **F:** SF measurements based on F1 and F0. Measuring the grating responses using F0 and F1 reveals that F0 predicts tuning to higher frequencies, with 27 units being more than 2 SF steps lower in their F1 tuning. **G:** original model output in response to LF and HF gratings over time for the phase-aligned model. HF responses sum temporally, the HF response is now again much larger than the LF envelope response. **H:** SF measurements based on F1 and F0 after phase-alignment. Across the population, this also aligns the preferred SF as estimated using F0 and F1 measures.

frequencies (Fig. 4C), indicative of a more complex-like cell that could detect high-frequency inputs. Plotting the outputs in response to different gratings over time revealed that for high-frequency gratings, individual filters were being driven most strongly, but that the output of each subunit did not coincide across time due to their different spatial locations. In contrast, to low-frequency gratings, the relatively small outputs of each subunit did overlap in time and summed (Fig. 4D). Therefore, the apparent selectivity to a low-SF grating was in fact

generated as a result of a low-SF “envelope” driving multiple high-SF features suboptimally, but simultaneously. Thus, this type of cell appears to be simple-like for low SFs, but complex for high SFs.

Indeed, this apparent discrepancy between subunit tuning and the tuning to gratings can be explained by the previously observed spatial scatter between filters. To demonstrate this, we simulated two models for each neuron, the original model of the data, along with a second model constructed with identical subunits, except that the filters of each



subunit were spatially aligned to have the same position, eliminating their spatial scatter (Fig. 4A, right). As expected, these peak-aligned models display greatly enhanced tuning to the carrier frequency (Fig. 4B, dotted lines) relative to the original models. Across our sample, peak alignment resulted in the model completely eliminating the striking discrepancy between model-based and simulated-grating-based estimates of SF tuning (Fig. 4F, paired  $t$  test,  $P = 0.0086$ ), resulting in the two measures closely in register with one another (Fig. 4H, paired  $t$  test,  $P = 0.4831$ ). In the context of classical F0/F1 measures, these results indicate that some cells may show large modulation in their F1 component at a lower frequency, while still having significant tuning to a higher SF that is obscured by the choice of gratings used, similar to some previously observed properties of complex cell responses (41). Thus, we interpret tuning at the envelope frequency as not being caused by the presence of an explicit envelope filter, but rather as arising from the interactions between individual, rectified, high-resolution filters.

### Quantifying the Degree of Nonlinearity across Cortical Layer

Model-based measures can also be useful to identify the degree that a given V1 neuron is nonlinear in its spatiotemporal processing. Traditionally, nonlinearity in V1 processing is referenced to the distinction between simple (relatively linear) and complex cells (nonlinear) (1, 42, 43), usually estimated from the F1/F0 ratios described earlier. In such characterizations, however, the degree of nonlinearity does not necessarily generalize across stimulus contexts (8, 14, 32, 44), and thus we propose alternative model-based measures that can be easily adjusted for use with arbitrary spatiotemporally varying stimuli.

We consider two time-varying spatiotemporal stimuli  $\mathbf{s}(t)$  and  $\tilde{\mathbf{s}}_x(t)$ , which are different only because the stimulus at position  $x$  is inverted (i.e., black instead of white and vice versa). By comparing the response of the neuron to both stimuli, we can gauge whether it has a linear (inverted) or nonlinear (same sign) response, analogously to how the neuron responds to opposite phases of a drifting grating. This motivates our definition of the spatial phase-reversal modulation sPRM( $x$ ):

$$\text{sPRM}(x) = \frac{1}{T} \sum_t \frac{|r[\mathbf{s}(t)] - r[\tilde{\mathbf{s}}_x(t)]|}{\bar{r}} \quad (3)$$

where  $\bar{r}$  is the firing response rate, and  $T$  is the total experiment duration. Notably, this is analogous to our previously proposed PRM measure (20), but provides spatial resolution across the receptive field, allowing for direct model-free validation using forward correlation.

Specifically, to validate the nonlinearity measurements provided by the sPRM( $x$ ), we measure the average response of the neuron across all instances in the experiment where a black bar was at position  $x$ , compared with when it was a white bar. The resulting phase-reversal forward correlation differences (PRFC, Fig. 5C) closely mirror the sPRM (Fig. 5B). In simple cells, presentation of white and black bars at the same spatial location is associated with opposite-sign modulation of firing rate relative to the firing rates elicited by gray bars, yielding overall PRFC values close to 1; in complex cells, either change

in luminance elicits the same response, causing the firing rates to sum and leaving the PRFC near 0 (Fig. 5C). Likewise, the distribution of PRFC values (Fig. 5D) shows a high prevalence of complex cells and reflects a bimodal distribution often seen in previous V1 cell classifications (42, 43, 45).

Like the PRM, the average PRFC (average weighted across the receptive field of the neuron) can also be used to summarize the overall degree of nonlinearity of the neuron. As expected, these two overall measures of nonlinearity also closely corresponded; we found significant agreement between the two measures (Fig. 5E), further validating the PRM and sPRM measures.

To demonstrate the utility of such model-based measures of nonlinearity, we computed the degree of nonlinearity across cortical layers, expecting increasing degrees of nonlinearity outside the input layers of V1 (layer IV). The PRFC measure of phase-invariance displays the expected distribution across cortical layers, with cells in layer IV having large values on this indicator of phase-invariance, indicating more simple-like cells, whereas extragranular layers show significantly lower values more associated with complex-like cells (Fig. 6A) (44, 46, 47). Notably, both simple and complex cells can have a large number of subunits, indicating that simple cells still typically have nonlinear processing (11, 48). Finally, we also compared model features across layer. Notably, our models also featured an additional aspect of infra-granular cells; their temporal kernels display longer onset latencies on average compared with layer IV cells (Fig. 6B) as previously described (49, 50).

## DISCUSSION

We have demonstrated how model-based characterizations of V1 neurons offer a more sophisticated description of their visual processing that is consistent with—but goes beyond—classical measures of V1 selectivity. Indeed, the underlying motivation is that nonlinear statistical models that are fit to more complex spatiotemporal stimuli capture aspects of V1 selectivity that are not evident in their responses to simpler stimuli, and thus measures based on such models will necessarily provide more information. Similarly, classical measures may not be possible where the stimulus cannot be precisely controlled, as is the case in an increasing number of experiments performed in awake animals in more natural contexts (51–53). Model-based characterization bridges the gap between recent advances in statistical modeling of neuron responses to complex stimuli (8) and the descriptions of V1 tuning established by classical stimuli. Thus, it can fill an important gap in relating what can be relatively uninterpretable, complex models to the fundamental stimulus selectivity of the modeled neurons. As such, we propose this approach as a new benchmark for describing V1 neuron selectivity that is applicable to its processing of complex stimuli.

We have illustrated such measures, and their implications, using an established nonlinear modeling framework (15). Much of our analysis relies on our model's ability to identify a given neuron's selectivity as a function of multiple subunits, as opposed to a single receptive field filter. Based on our analyses, most V1 neurons exhibit a diversity of subunit selectivity, in that individual cells are well described by many

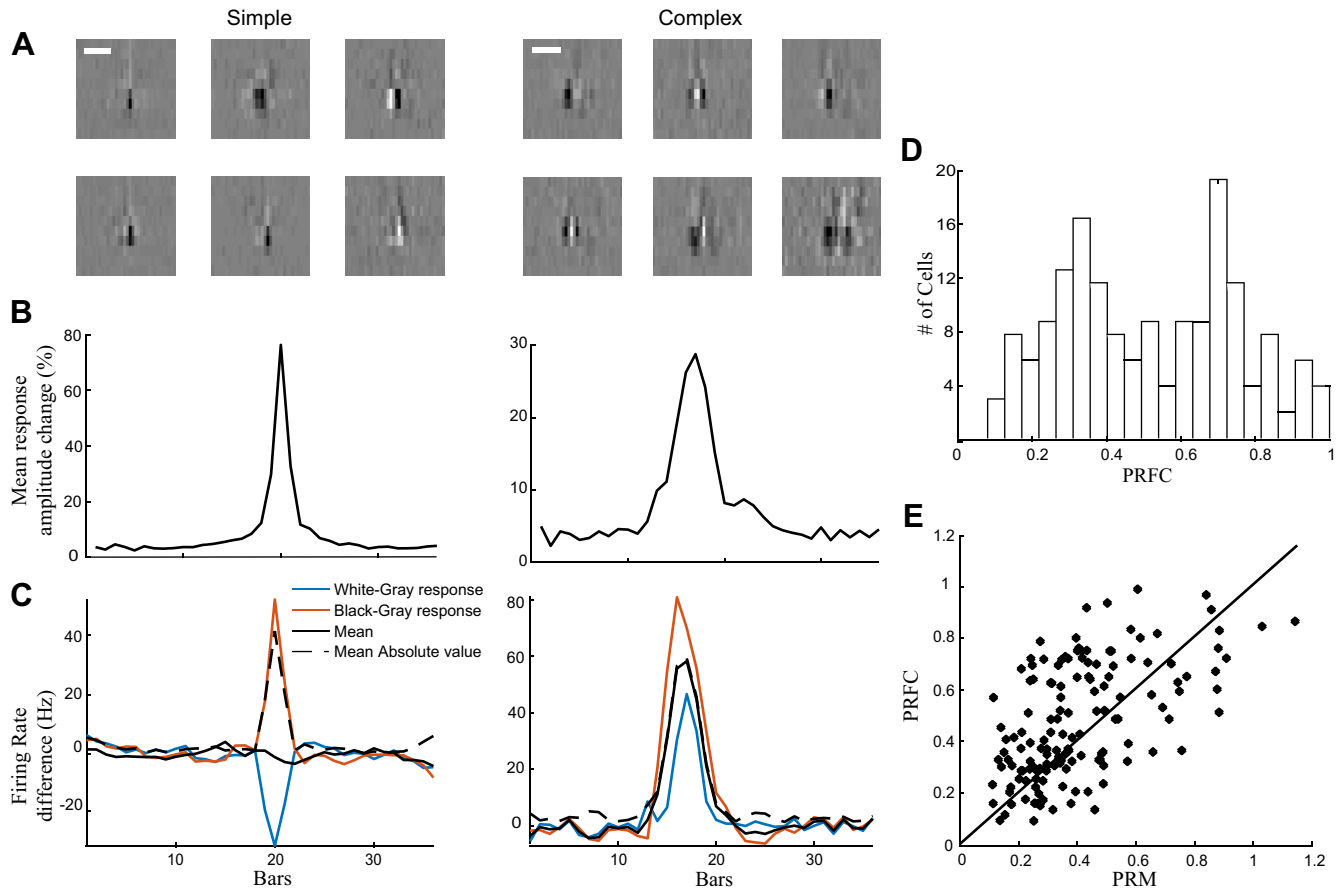


**Figure 5.** Measures of cell complexity and nonlinearity. *A*: example filters of a simple cell (*left*) and a complex cell (*right*). *B*: spatial phase-reversal modulation (PRM) profiles for the above cells. These spatial profiles closely match those established by the model filters in *A*. *C*: the spatial profiles of the forward-correlation based measure of phase insensitivity (phase-reversal forward correlation differences, PRFC) corresponding to the above example cells. Triggering on each instance of a bar at one spatial position being non-gray yields a measure of firing rate modulation across space. For a simple cell (*left*), responses to bars of the opposite sign are also opposite, leading them to average out relative to the average of their absolute values. In a complex cell (*right*), any non-gray bar increases the firing rate, leaving the average modulation identical to the average of its absolute values. *D*: histogram of PRFC values, showing the broadly bimodal distribution normally associated with the simple/complex spectrum. *E*: agreement between model-based and model-free measures of cell complexity.

subunits that are often selective to multiple distinct spatiotemporal elements. For example, some V1 neurons might combine direction-selective subunits with those tuned to nonmoving features (such as the example model in Fig. 1C, where only subunit 6 is direction-selective). Our results thus not only highlight the diversity of selectivity known to be exhibited by V1 neurons but also emphasize the need for model-based characterization to understand this diversity.

Furthermore, the approaches presented here can be applied to any model of V1 whose first stage consists of multiple spatiotemporal processing elements and otherwise is image-computable (e.g., generates a predicted response to stimulus input), and thus in principle can be applied to the range of models from spike-triggered neural characterization (e.g., see Refs. 11, 12, and 28) to more recent models based on deep neural networks (e.g., see Refs. 13 and 54–58), as the first stage of many such networks likely approximates a similar dimensionality reduction process as our filter subspace approach. However, we expect that such characterizations will be most accurate in models that accurately capture the neural computations (i.e., have high predictive power) and

spatiotemporal processing attributable to individual V1 neurons, and thus use the NIM (14, 15) in this paper for the basis of these characterizations.

A key finding of our analyses is that multiple subunits conferred tuning to a broader range of stimulus properties than would have been observable under classical contexts using traditional analyses. In the case of spatial frequency tuning, we find that some cells, although capable of resolving high-resolution inputs as indicated by the SF tuning of their subunits, are also tuned to broader stimulation by low-resolution inputs that spread across the cell's entire RF. This also potentially offers an explanation of how complex cells can still show some phase-selective response patterns when presented with low-frequency gratings moving across the receptive field, while stationary gratings failed to elicit the same response, and explains the previously demonstrated dependence of the classical F1/F0 measure on spatial frequency (41). These findings are also consistent with findings of envelope tuning (59, 60), in which V1 processing for boundary segmentation is described as a theoretical LNLN cascade-style model with high-frequency filters in the first

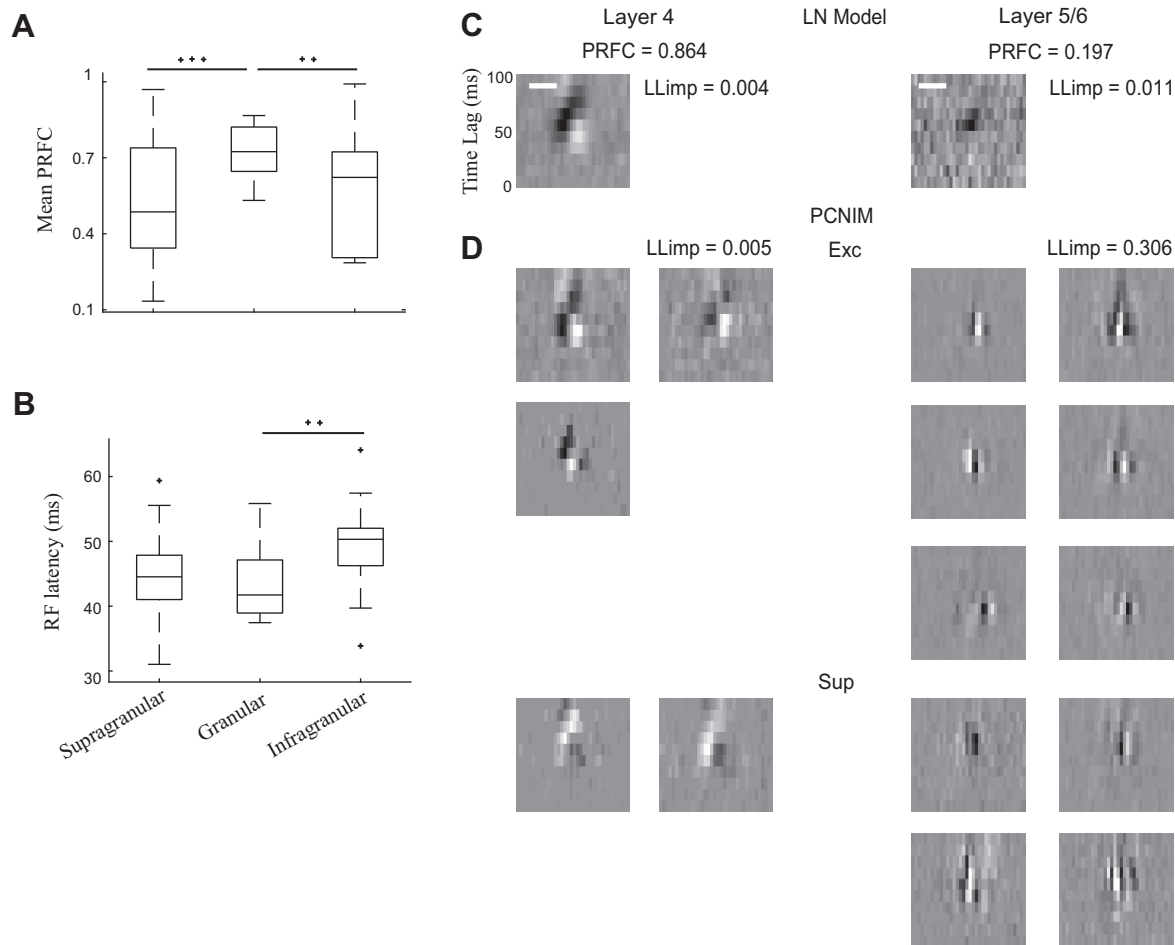


**Figure 6.** Degree of nonlinearity across cortical layer. **A:** phase-reversal forward correlation differences (PRFC) across the recorded population, revealing that neurons in layer 4 are less nonlinear (have large PRFC values), while infra- and supra granular cells are more nonlinear (small PRFC values), indicating a much higher proportion of complex cells in those layers. **B:** mean latency of excitatory filters for each model. Cells from infragranular layers have slower onsets, indicating that our models capture a delay in processing onset. The + symbols indicate significance at 0.05 (+), 0.01 (++), and 0.001 (+++) levels. **C and D:** example linear-nonlinear (LN) (in **C**) and principal component nonlinear input model (PCNIM) (in **D**) fits for a layer 4 simple cell (*left*) and a layer 5/6 complex cell (*right*) with both excitatory (Exc) and suppressive (Sup) filters. The PCNIM provides only a modest benefit in log-likelihood improvement (LLimp) for the simple cell, but a massive improvement for the complex cell. Beyond having a greater number of filters and being able to fit the phase-invariant complex cell, the PCNIM reveals additional high-resolution receptive field (RF) structure in both cases.

LN step and a coarse-scale boundary determined by the second LN step. They similarly observed responses to high-SF stimuli when presenting contrast-reversing luminance gratings (59), implying that the ternary bar stimuli used in this study likely drives V1 activity in similar ways. However, unlike their model, we did not observe a single filter outlining the envelope, but instead find that the response to the low-frequency envelope emerges out of the combined contribution of many more localized filters that are spatially scattered around the cell's RF.

In addition, our model filters capture the high-resolution components of the cell RF as predicted by that study and thus provide a way of quantifying the differences between tuning to envelope and carrier frequencies of a visual signal. Because related theoretical work (61) found that scattered high-frequency inputs may also be indicative of cells with broad orientation tuning, the interaction between subunit scatter and orientation tuning will need to be investigated in the future using stimuli with more dimensions than those

used in our study, such as bar stimuli presented at multiple orientations or two-dimensional noise stimuli. Such an approach might also yield clearer insight into other tuning properties where we observed significant variability between subunits, such as direction selectivity.

Our model-based approach also allows us to investigate the degree of nonlinearity needed to capture the responses of different V1 populations despite the well-established diversity of nonlinearity and tuning properties of primary visual cortex (42, 62, 63) at much higher spatial resolution than was previously possible. Our model-based measures demonstrate a bimodal distribution of the degree of nonlinearity (5, 42) and allows for additional insight into the construction of phase-invariant RFs by showing the spatial extent of individual subunits and their overlap. Because of this increased spatial resolution, the utility of our models as a measure of phase-invariance thus also goes beyond what is possible with classical analyses, such as using relative modulation analysis after presenting grating stimuli (27). A key point to

emphasize is that it is only possible to study the effects of nonlinear interactions across space in the context of sufficiently complex stimuli. Our analyses of the resulting models could focus on interactions between filters at the same spatial position, which appear to be the real mark of whether the cell exhibits linear “simple-cell-like” stimulus processing or spatial-phase invariant “complex-cell-like” processing.

Likewise, simpler measures such as the number of subunits is not a reliable indicator of cell complexity [consistent with previous modeling studies (11, 13, 15, 16, 48)]. Indeed, we see that the smaller scale of spatial selectivity relative to the full RF of the neuron can require multiple filters regardless of whether neurons are phase-invariant. However, how this scale difference manifests depends on the assumptions of modeling; techniques such as spike-triggered covariance will often explain the “most variance” of the subunit ensemble with large quadrature pair filters (11, 18, 28) and leave finer elements of spatial selectivity to later filters—but such characterizations are consistent with small, localized filters (29). Indeed, statistical models that have flexibility in their nonlinear processing, which for example is afforded by rectified subunits (8, 15, 31) not only can better capture neural responses but also offer a finer description of such nonlinear interactions.

We propose that our approach for model-based measures provides a new benchmark for quantitative estimation and comparison of tuning properties. The investigation of differences between neurons across cortical lamina is just one application of our approach—future experiments may make comparisons between other neural populations, such as across eccentricity or between CO blobs, to probe the functional organization of the visual cortex by identifying which computational subunits change in different contexts. Furthermore, although we used relatively low-dimensional bar stimuli, the approach is applicable to responses to any complex stimuli, including more natural stimuli that vary in additional dimensions such as color and stimulus contrast. Indeed, while probing more stimulus dimensions requires more data to support the resulting models (8), models fit using those stimuli could reveal how such properties integrate with the selectivity measures described in this paper. Likewise, model-based characterizations might similarly be applied to “deeper” models with additional stages of nonlinear processing than the two LN stages we used here (8, 13, 31, 56, 57, 64), either to describe later regions in the visual system or to further explore the additional nonlinearities present in V1. Such deeper networks would also be a more powerful tool to accurately identify shared computation in the context of more complex, and thus more high-dimensional, stimuli. Finally, due to the structural similarities among sensory cortical areas, model-based characterization might be further adapted to auditory or somatosensory modalities, potentially providing insight into general processing patterns in cortex by allowing for more direct comparison of shared or distinct computational subunits.

## APPENDIX

Figure A1 shows the components and performance of the principal component nonlinear input model.

## GRANTS

D.A.B. and F.B. were supported by NEI/NIH Grant EY025403. F.B. was partially supported by NSF award DGE-1632976. B.G.C. was supported by the Intramural research program at NEI/NIH.

## DISCLOSURES

No conflicts of interest, financial or otherwise, are declared by the authors.

## AUTHOR CONTRIBUTIONS

B.G.C. and D.A.B. conceived and designed research; B.G.C. performed experiments; F.B. analyzed data; F.B. and D.A.B. interpreted results of experiments; F.B. prepared figures; F.B. drafted manuscript; F.B., B.G.C., and D.A.B. edited and revised manuscript; F.B., B.G.C., and D.A.B. approved final version of manuscript.

## REFERENCES

- Hubel DH, Wiesel TN. Receptive fields, binocular interaction and functional architecture in the cat's visual cortex. *J Physiol* 160: 106–154, 1962. doi:10.1113/jphysiol.1962.sp006837.
- Alonso J-M, Martinez LM. Functional connectivity between simple cells and complex cells in cat striate cortex. *Nat Neurosci* 1: 395–403, 1998. doi:10.1523/JNEUROSCI.2665-13.2013.
- Maunsell JHR, Newsome WT. Visual processing in monkey extrastriate cortex. *Annu Rev Neurosci* 10: 363–401, 1987. doi:10.1146/annurev.ne.10.030187.002051.
- Movshon JA, Thompson ID, Tolhurst DJ. Spatial and temporal contrast sensitivity of neurones in areas 17 and 18 of the cat's visual cortex. *J Physiol* 283: 101–120, 1978. doi:10.1113/jphysiol.1978.sp012490.
- Chen Y, Anand S, Martinez-Conde S, Macknik SL, Bereshpolova Y, Swadlow HA, Alonso JM. The linearity and selectivity of neuronal responses in awake visual cortex. *J Vis* 9: 12–12, 2009. doi:10.1167/9.9.12.
- DeAngelis GC, Freeman RD, Ohzawa I. Length and width tuning of neurons in the cat's primary visual cortex. *J Neurophysiol* 71: 347–374, 1994. doi:10.1152/jn.1994.71.1.347.
- Sceniak MP, Ringach DL, Hawken MJ, Shapley R. Contrast's effect on spatial summation by macaque V1 neurons. *Nat Neurosci* 2: 733–739, 1999. doi:10.1038/11197.
- Butts DA. Data-driven approaches to understanding visual neuron activity. *Annu Rev Vis Sci* 5: 451–477, 2019. doi:10.1146/annurev-vision-091718-014731.
- David SV, Gallant JL. Predicting neuronal responses during natural vision. *Network* 16: 239–260, 2005. doi:10.1080/09548980500464030.
- Sharpee TO. Computational identification of receptive fields. *Annu Rev Neurosci* 36: 103–120, 2013. doi:10.1146/annurev-neuro-062012-170253.
- Rust NC, Schwartz O, Movshon JA, Simoncelli EP. Spatiotemporal elements of macaque V1 receptive fields. *Neuron* 46: 945–956, 2005. doi:10.1016/j.neuron.2005.05.021.
- Touryan J, Lau B, Dan Y. Isolation of relevant visual features from random stimuli for cortical complex cells. *J Neurosci* 22: 10811–10818, 2002. doi:10.1523/JNEUROSCI.22-24-10811.2002.
- Cadena SA, Denfield GH, Walker EY, Gatys LA, Tolias AS, Bethge M, Ecker AS. Deep convolutional models improve predictions of macaque V1 responses to natural images. *PLoS Comput Biol* 15: e1006897, 2019. doi:10.1371/journal.pcbi.1006897.
- Almasi A, Meffin H, Cloherty SL, Wong Y, Yunzab M, Ibbotson MR. Mechanisms of feature selectivity and invariance in primary visual cortex. *Cereb Cortex* 30: 5067–5087, 2020. doi:10.1093/cercor/bhaa102.
- McFarland JM, Cui Y, Butts DA. Inferring nonlinear neuronal computation based on physiologically plausible inputs. *PLoS Comput Biol* 9: e1003143, 2013. doi:10.1371/journal.pcbi.1003143.
- Park M, Pillow JW. Receptive field inference with localized priors. *PLoS Comput Biol* 7: e1002219, 2011. doi:10.1371/journal.pcbi.1002219.
- Vintch B, Movshon JA, Simoncelli EP. A convolutional subunit model for neuronal responses in macaque V1. *J Neurosci* 35: 14829–14841, 2015. doi:10.1523/JNEUROSCI.2815-13.2015.



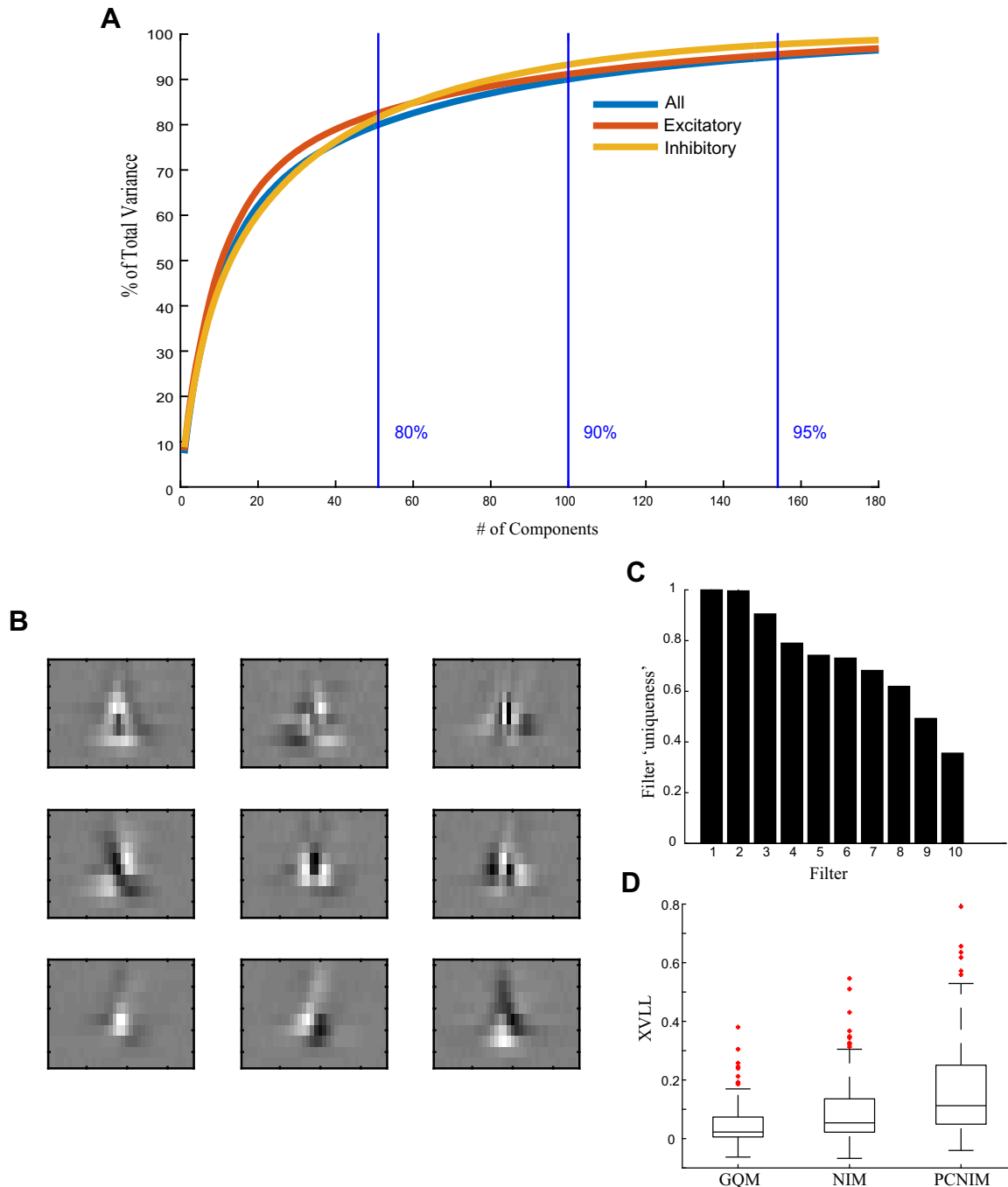


**Figure A1.** The principal component nonlinear input model (PCNIM). **A:** variance explained by each principal component of a filter bank consisting of 1,528 excitatory and 487 inhibitory filters. Eighty percent of the total variance is explained by 51 PCs, 90% is explained by 100 PCs, and 95% is explained by 154 PCs. **B:** first nine principal components used for dimensionality reduction during modeling. **C:** “uniqueness” of each filter of the example model shown in Fig. 1C, quantified by the filter’s vector magnitude after orthogonalizing it from the previous filters with the Gram–Schmidt process. Most filters make significant contributions to outlining a different area of stimulus space the cell responds to. **D:** log-likelihood improvement of the models using the PC-space for dimensionality reduction relative to full-space models. The PCNIM clearly outperforms other models—the quadratic model (GQM) and the full-space nonlinear input model (NIM)—in describing the observed data in terms of cross-validated log-likelihood (XVLL).

18. **Park IM, Archer E, Priebe N, Pillow JW.** Spectral methods for neural characterization using generalized quadratic models. *Adv Neural Inf Process Syst* 26: 2454–2462, 2013.
19. **Vintch B, Zaharia AD, Movshon JA, Simoncelli EP.** Efficient and direct estimation of a neural subunit model for sensory coding. *Adv Neural Inf Process Syst* 25: 3113–3121, 2012.
20. **McFarland JM, Bondy AG, Cumming BG, Butts DA.** High-resolution eye tracking using V1 neuron activity. *Nat Commun* 5: 4605, 2014. doi:10.1038/ncomms5605.
21. **McFarland JM, Cumming BG, Butts DA.** Variability and correlations in primary visual cortical neurons driven by fixational eye movements. *J Neurosci* 36: 6225–6241, 2016. doi:10.1523/JNEUROSCI.4660-15.2016.

22. **Chen Y, Dhamala M, Bollimunta A, Schroeder CE, Ding M.** Current source density analysis of ongoing neural activity: theory and application. *NeuroMethods* 54: 27–40, 2011. doi:10.1007/978-1-60327-202-5\_2.
23. **Pettersen KH, Devor A, Ulbert I, Dale AM, Einevoll GT.** Current-source density estimation based on inversion of electrostatic forward solution: effects of finite extent of neuronal activity and conductivity discontinuities. *J Neurosci Methods* 154: 116–133, 2006. doi:10.1016/j.jneumeth.2005.12.005.
24. **Adelson EH, Bergen JR.** Spatiotemporal energy models for the perception of motion. *J Opt Soc Am A* 2: 284–299, 1985. doi:10.1364/josaa.2.000284.
25. **Mante V, Carandini M.** Mapping of stimulus energy in primary visual cortex. *J Neurophysiol* 94: 788–798, 2005. doi:10.1152/jn.01094.2004.
26. **Carandini M, Heeger DJ, Movshon JA.** Linearity and normalization in simple cells of the macaque primary visual cortex. *J Neurosci* 17: 8621–8644, 1997. doi:10.1523/JNEUROSCI.17-21-08621.1997.
27. **Kagan I, Gur M, Snodderly DM.** Spatial organization of receptive fields of V1 neurons of alert monkeys: comparison with responses to gratings. *J Neurophysiol* 88: 2557–2574, 2002. doi:10.1152/jn.00858.2001.
28. **Touryan J, Felsen G, Dan Y.** Spatial structure of complex cell receptive fields measured with natural images. *Neuron* 45: 781–791, 2005. doi:10.1016/j.neuron.2005.01.029.
29. **Lochmann T, Blanche TJ, Butts DA.** Construction of direction selectivity through local energy computations in primary visual cortex. *PLoS One* 8: e58666, 2013. doi:10.1371/journal.pone.0058666.
30. **Haider B, Häusser M, Carandini M.** Inhibition dominates sensory responses in the awake cortex. *Nature* 493: 97–100, 2012. doi:10.1038/nature11665.
31. **Kriegeskorte N.** Deep neural networks: a new framework for modeling biological vision and brain information processing. *Annu Rev Vis Sci* 1: 417–446, 2015. doi:10.1146/annurev-vision-082114-035447.
32. **Ringach D, Shapley R.** Reverse correlation in neurophysiology. *Cogn Sci* 28: 147–166, 2004. doi:10.1016/j.cogsci.2003.11.003.
33. **Spratling MW.** Predictive coding accounts for V1 response properties recorded using reverse correlation. *Biol Cybern* 106: 37–49, 2012. doi:10.1007/s00422-012-0477-7.
34. **Tanabe S, Cumming BG.** Delayed suppression shapes disparity selective responses in monkey V1. *J Neurophysiol* 111: 1759–1769, 2014. doi:10.1152/jn.00426.2013.
35. **Ringach DL, Hawken MJ, Shapley R.** Dynamics of orientation tuning in macaque V1: the role of global and tuned suppression. *J Neurophysiol* 90: 342–352, 2003. doi:10.1152/jn.01018.2002.
36. **Taylor MM, Contreras D, Destexhe A, Frégnac Y, Antolik J.** An anatomically constrained model of V1 simple cells predicts the coexistence of push-pull and broad inhibition. *J Neurosci* 41: 7797–7812, 2021. doi:10.1523/JNEUROSCI.0928-20.2021.
37. **Mazer JA, Vinje WE, McDermott J, Schiller PH, Gallant JL.** Spatial frequency and orientation tuning dynamics in area V1. *Proc Natl Acad Sci USA* 99: 1645–1650, 2002. doi:10.1073/pnas.022638499.
38. **Priebe NJ, Ferster D.** Direction selectivity of excitation and inhibition in simple cells of the cat primary visual cortex. *Neuron* 45: 133–145, 2005. doi:10.1016/j.neuron.2004.12.024.
39. **Ninomiya T, Sanada TM, Ohzawa I.** Contributions of excitation and suppression in shaping spatial frequency selectivity of V1 neurons as revealed by binocular measurements. *J Neurophysiol* 107: 2220–2231, 2012. doi:10.1152/jn.00832.2010.
40. **Victor JD, Purpura K, Katz E, Mao B.** Population encoding of spatial frequency, orientation, and color in macaque V1. *J Neurophysiol* 72: 2151–2166, 1994. doi:10.1152/jn.1994.72.5.2151.
41. **Movshon JA, Thompson ID, Tolhurst DJ.** Receptive field organization of complex cells in the cat's striate cortex. *J Physiol* 283: 79–99, 1978. doi:10.1113/jphysiol.1978.sp012489.
42. **Mechler F, Ringach DL.** On the classification of simple and complex cells. *Vision Res* 42: 1017–1033, 2002. doi:10.1016/s0042-6989(02)00025-1.
43. **Skottun BC, De Valois RL, Grosz DH, Movshon JA, Albrecht DG, Bonds AB.** Classifying simple and complex cells on the basis of response modulation. *Vision Res* 31: 1078–1086, 1991. doi:10.1016/0042-6989(91)90033-2.
44. **Yeh CI, Xing D, Williams PE, Shapley RM.** Stimulus ensemble and cortical layer determine V1 spatial receptive fields. *Proc Natl Acad Sci USA* 106: 14652–14657, 2009 [Erratum in *Proc Natl Acad Sci USA* 106: 16890, 2009]. doi:10.1073/pnas.0907406106.
45. **Priebe NJ, Mechler F, Carandini M, Ferster D.** The contribution of spike threshold to the dichotomy of cortical simple and complex cells. *Nat Neurosci* 7: 1113–1122, 2004. doi:10.1038/nn1310.
46. **Atencio CA, Sharpee TO, Schreiner CE.** Receptive field dimensionality increases from the auditory midbrain to cortex. *J Neurophysiol* 107:2594–2603, 2012. doi:10.1152/jn.01025.2011.
47. **Sharpee TO, Atencio CA, Schreiner CE.** Hierarchical representations in the auditory cortex. *Curr Opin Neurobiol* 21: 761–767, 2011. doi:10.1016/j.conb.2011.05.027.
48. **Fournier J, Monier C, Levy M, Marre O, Sári K, Kisvárdy ZF, Frégnac Y.** Hidden complexity of synaptic receptive fields in cat V1. *J Neurosci* 34: 5515–5528, 2014. doi:10.1523/JNEUROSCI.0474-13.2014.
49. **McFarland JM, Bondy AG, Saunders RC, Cumming BG, Butts DA.** Saccadic modulation of stimulus processing in primary visual cortex. *Nat Commun* 6: 8110, 2015. doi:10.1038/ncomms9110.
50. **Nowak LG, Munk MHJ, Girard P, Bullier J.** Visual latencies in areas V1 and V2 of the macaque monkey. *Vis Neurosci* 12: 371–384, 1995. doi:10.1017/s095252380000804x.
51. **Michaël AM, Abe ETT, Niell CM.** Dynamics of gaze control during prey capture in freely moving mice. *eLife* 9: 1–27, 2020. doi:10.7554/eLife.57458.
52. **Miller CT, Gire D, Hoke K, Huk AC, Kelley D, Leopold DA, Smear MC, Theunissen F, Yartsev M, Niell CM.** Natural behavior is the language of the brain. *Curr Biol* 32: R482–R493, 2022. doi:10.1016/j.cub.2022.03.031.
53. **Yates JL, Coop SH, Sarch GH, Wu R-J, Butts DA, Rucci M, Mitchell JF.** Beyond Fixation: detailed characterization of neural selectivity in free-viewing primates (Preprint). *bioRxiv*, 2021. <https://doi.org/10.1101/2021.11.06.467566>.
54. **Kindel WF, Christensen ED, Zylberberg J.** Using deep learning to reveal the neural code for images in primary visual cortex. *J Vis* 19: 29, 2017. doi:10.1167/19.4.29.
55. **Klindt DA, Ecker AS, Euler T, Bethge M.** Neural system identification for large populations separating “what” and “where.” *Adv Neural Inf Process Syst* 30: 3507–3517, 2017.
56. **Lurz K-K, Bashiri M, Willeke K, Jagadish AK, Wang E, Walker EY, Cadena SA, Muhammad T, Cobos E, Tolias AS, Ecker AS, Sinz FH.** Generalization in data-driven models of primary visual cortex (Preprint). *bioRxiv*, 2021. doi:10.1101/2020.10.05.326256.
57. **Moskowitz TH, Roy NA, Pillow JW.** A comparison of deep learning and linear-nonlinear cascade approaches to neural encoding (Preprint). *bioRxiv*, 2018. <https://doi.org/10.1101/463422>.
58. **Ustyuzhaninov I, Cadena SA, Froudarakis E, Fahey PG, Walker EY, Cobos E, Reimer J, Sinz FH, Tolias AS, Bethge M, Ecker AS.** Rotation-invariant clustering of neuronal responses in primary visual cortex. 8th International Conference on Learning Representations, ICLR 2020, Addis Ababa, Ethiopia, April 26–30, 2020, p. 1–3.
59. **Gharat A, Baker CL.** Nonlinear Y-like receptive fields in the early visual cortex: an intermediate stage for building cue-invariant receptive fields from subcortical Y cells. *J Neurosci* 37: 998–1013, 2017. doi:10.1523/JNEUROSCI.2120-16.2016.
60. **Zavitz E, Baker CL.** Higher order image structure enables boundary segmentation in the absence of luminance or contrast cues. *J Vis* 14: 14, 2014. doi:10.1167/14.4.14.
61. **Li G, Talebi V, Yoonessi A, Baker CL.** A FPGA real-time model of single and multiple visual cortex neurons. *J Neurosci Methods* 193: 62–66, 2010. doi:10.1016/j.jneumeth.2010.07.031.
62. **Goris RLT, Simoncelli EP, Movshon JA.** Origin and function of tuning diversity in macaque visual cortex. *Neuron* 88:819–831, 2015. doi:10.1016/j.neuron.2015.10.009.
63. **Talebi V, Baker CL.** Categorically distinct types of receptive fields in early visual cortex. *J Neurophysiol* 115: 2556–2576, 2016. doi:10.1152/jn.00659.2015.
64. **Richards BA, Lillicrap TP, Beaudoin P, Bengio Y, Bogacz R, Christensen A, et al.** A deep learning framework for neuroscience. *Nat Neurosci* 22: 1761–1770, 2019. doi:10.1038/s41593-019-0520-2.